

# Personalized visual encoding model construction with small data

Zijin Gu<sup>1</sup>, Keith Jamison<sup>2</sup>, Mert Sabuncu<sup>1,2</sup>, and Amy Kuceyeski<sup>2,\*</sup>

<sup>1</sup>School of Electrical and Computer Engineering, Cornell University, Ithaca, New York, USA

<sup>2</sup>Department of Radiology, Weill Cornell Medicine, New York, New York, USA

\*amk2012@med.cornell.edu

## ABSTRACT

Measuring and modeling individual-level differences in brain responses to external stimuli, e.g. images, video or sound, is an area of increasing interest in neuroscience. Quantifying population heterogeneity in stimuli-response mapping may allow insight into variability in bottom-up neural systems that can in turn be related to individual's behavior or pathological state. Encoding models that predict brain response patterns to stimuli are one way to capture this relationship, however, they generally need a large amount of training data to achieve optimal accuracy. Thus, creating an encoding model for a specific individual can require significant resources be devoted to data collection and processing. Here, we propose and test an alternative personalized ensemble encoding model approach to utilize existing encoding models, trained on deeply-sampled data from several individuals, to create encoding models for novel individuals with relatively little stimuli-response data. We show that these personalized ensemble encoding models trained with small amounts of data for a specific individual, i.e. 400 image-response pairs, achieve accuracy not different from models trained on 24,000 image-response pairs for the same individual. Importantly, the personalized ensemble encoding models preserve patterns of inter-individual variability in the image-response relationship. Additionally, we use our personalized ensemble encoding model within the recently developed NeuroGen framework to generate optimal stimuli designed to maximize specific regions' activations for a specific individual. We show that the inter-individual differences in face area responses to images of dog vs human faces observed previously is replicated using NeuroGen with the ensemble encoding model. Finally, and most importantly, we show the proposed approach is robust against domain shift by validating on a prospectively collected set of image-response data in novel individuals with a different scanner and experimental setup. Our approach shows the potential to use previously collected, deeply sampled data to efficiently create accurate, personalized encoding models and, subsequently, personalized optimal synthetic images for new individuals scanned under different experimental conditions.

**Keywords:** neural encoding model, vision neuroscience, generative networks, functional MRI

### Highlights:

- We propose a linear ensemble modeling approach for obtaining a personalized visual encoding model using small data, i.e. a few hundred image-response pairs, that performs comparably to encoding models trained on large data, i.e. 24K image-response pairs.
- We show that the prediction accuracy of the linear ensemble models are equivalent to the full encoding models, while still largely preserving the original patterns of individual variability in brain response patterns.
- The synthetic images generated from NeuroGen using the linear ensemble models can well represent the images generated from NeuroGen using the full encoding models, including preservation of inter-individual differences in image content that maximally activates a given visual region.
- We demonstrate that the accuracy of the linear ensemble encoding model approach is robust to several types of domain shifts, although the level of robustness varies according to the visual region.

## 1 Introduction

Neural encoding models of vision that approximate brain responses to images have gained popularity in human studies with the wide-spread adoption of non-invasive functional MRI (fMRI) techniques<sup>1</sup> and recent advances in large-scale publicly available fMRI datasets of human responses to visual stimuli<sup>2</sup>. These neuroscientific resources have become available at a time of ubiquitous deep learning applications in every aspect of science and technology, but particularly in image analysis<sup>3-8</sup>. Recent

work has revealed some agreement between image representations in biological and artificial neural networks (ANNs)<sup>9</sup>. This is somewhat unsurprising, as ANNs were originally inspired by the principles of how the feed-forward cortical network processes visual information<sup>10,11</sup>. Understanding how the human brain, unarguably the most efficient and adaptable learning system in the known universe, processes incoming information will no doubt lead to breakthroughs in neuroscience and artificial intelligence alike.

The functions and response properties of the visual cortex, with its central evolutionary role and ease of experimental perturbation, have been extensively studied<sup>12–16</sup>. Regions that respond to evolutionarily important content, like faces, bodies and places are relatively consistent across different individuals in their existence and spatial locations within the brain. Other regions, like those that respond to evolutionarily later content, like text/words, are more variable across individuals and are more experience dependent<sup>17</sup>. Recent work, including ours, has focused on investigating inter-individual differences in how brains process incoming stimuli<sup>18</sup>. One paper in particular revealed variations in neural and behavioral responses to auditory stimuli that are related to an individual's level of paranoia<sup>19</sup> while another showed that measuring brain responses to naturalistic stimuli (movie) could amplify inter-individual variability in behaviorally relevant networks compared to task-free paradigms<sup>20</sup>.

There are an increasing number of densely-sampled fMRI datasets in existence which enable both predicting brain response from natural images and in turn, identifying natural images from brain activity patterns<sup>2,21,22</sup>. Accurate individual-level voxel-wise and region-wise encoding models can be created using thousands of training data provided by these datasets<sup>23–26</sup>. However, due to the excessive resources required to obtain large data from one individual, such experiments are usually restricted to less than 10 subjects and thus far cannot be used to predict a novel individual's responses. Population-level encoding models can be created by averaging densely-sampled individual encoding models or trained using pooled data from all subjects<sup>2,26</sup>; however, individual variability will be obscured using this approach. There is a clear need for a tool that can use previously collected densely-sampled data to efficiently create encoding models for a specific individual using small amounts of their own data.

In this work, we create and assess the accuracy of an ensemble encoding approach that uses existing individual encoding models pre-trained with densely-sampled data<sup>18,27</sup> to predict brain responses to visual stimuli in novel individuals. We quantify the specific number of image-response pairs that needs to be collected in the prospective individual to obtain accuracy similar to a densely-trained encoding model. We also aimed to test if the ensemble-linear model could be used within the NeuroGen framework to replicate the previously discovered inter-individual variability in a face area responses to dogs and humans<sup>18</sup>. Finally, and most importantly for practical reasons, we quantified the accuracy of our ensemble-linear model when applied to novel individuals undergoing several domain shifts in the data. If validated, this modeling approach could be used to efficiently and accurately create personalized encoding models and optimized synthetic images for individuals in prospective experiments designed to shed light on inter-individual variability in visual processing.

## 2 Materials and methods

### 2.1 Data description

#### 2.1.1 Natural Scenes Dataset

The individual encoding models were trained and tested on Natural Scenes Dataset (NSD)<sup>2</sup>, which contains densely-sampled functional MRI (fMRI) data from eight participants (6 female, age 19–32 years). Each subject viewed 9,000–10,000 distinct color natural scenes with 2–3 repeats per scene over the course of 30–40 7T MRI sessions (whole-brain gradient-echo EPI, 1.8-mm iso-voxel and 1.6s TR). The images that subjects viewed (3s on and 1s off) were from the Microsoft Common Objects in Context (COCO) database<sup>28</sup> with a square crop resized to  $8.4^\circ \times 8.4^\circ$ . Among all images, a set of 1,000 were shared across all subjects while the remaining images for each individual were mutually exclusive across subjects. Subjects were asked to fixate centrally and perform a long-term continuous image recognition task (inf-back) to encourage maintenance of attention.

The fMRI data were pre-processed to correct for slice time differences and head motion using temporal interpolation and spatial interpolation. Then the single-trial beta weights representing the voxel-wise response to the image presented was estimated using a general linear model (GLM). There are three steps for the GLM: the first is to estimate the voxel-specific hemodynamic response functions (HRFs); the second is to apply the GLMdenoise technique<sup>29,30</sup> to the single-trial GLM framework; and the third is to use an efficient ridge regression<sup>31</sup> to regularize and improve the accuracy of the beta weights, which represent activation in response to the image. FreeSurfer was used to reconstruct the cortical surface, and both volume- and surface-based versions of the voxel-wise response maps were created. The fLoc data was used to create contrast maps (voxel-wise t-statistics) of responses to specific object categories, and region boundaries were then manually drawn on inflated surface maps by identifying contiguous regions of high contrast in the expected cortical location, and thresholding to include all vertices with contrast  $> 0$  within that boundary. Early visual ROIs were defined manually using retinotopic mapping data on the cortical surface. Surface-defined ROIs were projected back to fill in voxels within the gray matter ribbon. Region-wise image responses were then calculated by averaging the voxel-wise beta response maps over all voxels within a given region.

## 2.1.2 NeuroGen Dataset

To further prove the proposed encoding models are robust against domain shift and translatable to novel individuals, we collected prospective data we are calling the NeuroGen dataset. Six individuals (5 female, age 19-25) underwent MRI, including an anatomical T1 scan (0.9 mm iso-voxel), a functional category localizer to identify higher-order visual region boundaries (as in the NSD acquisition), and, finally, an fMRI while viewing a fixed set of 480 images. Two-hundred and forty of the images were selected from the union of all images shown to the NSD subjects and 240 were synthetic images created by NeuroGen<sup>18</sup>, a generative framework that can create synthetic images within a given image category. The task fMRI experimental setup was replicated as closely as possible to the NSD setup, i.e. the images were square cropped and resized to  $8.4^\circ \times 8.4^\circ$  and were presented for 3s on and 1s off. Data were acquired on a GE MR750 3T scanner. fMRI data consisted of posterior oblique-axial slices oriented to capture early visual areas and the ventral visual stream (gradient-echo EPI,  $2.25 \times 2.25 \times 3.00$ mm, 27 interleaved slices, TR=1.45s, TE=32ms, phase-encoding in the A»P direction). EPI susceptibility distortion was estimated using pairs of spin-echo scans with reversed phase-encoding directions<sup>32</sup>. Preprocessing included slice-timing correction with upsampling to 1 second TR, followed by a single-step spatial interpolation combining motion, distortion, and resampling to 2mm isotropic voxels.

## 2.2 Encoding models

### 2.2.1 Deepnet feature-weighted receptive field encoding models

Figure 1 illustrates the Deepnet feature-weighted receptive field (Deepnet-fwRF) encoding model architecture, which takes an input image and predicts a particular visual region's response to that image. There are three components to the Deepnet-fwRF model: image features, region-specific Gaussian pooling fields and weights of the pooled image features. The image feature maps are derived from the convolutional layers and fully-connected layers in pretrained Alexnet<sup>3,33</sup>, which were then dimension-reduced to only contain 512 feature maps per layer by selecting those having the highest explained variance across the whole NSD image set. To further reduce dimensionality of the feature maps while taking into account the specificity of the receptive field of each region, a region-specific Gaussian pooling field with center and radius obtained via grid search was applied to each map. Finally, feature weights for each pooled feature map value were learned through ridge regression. Detailed information on the model framework can be found in previous work<sup>18,27</sup>.

### Deepnet-fwRF encoding model

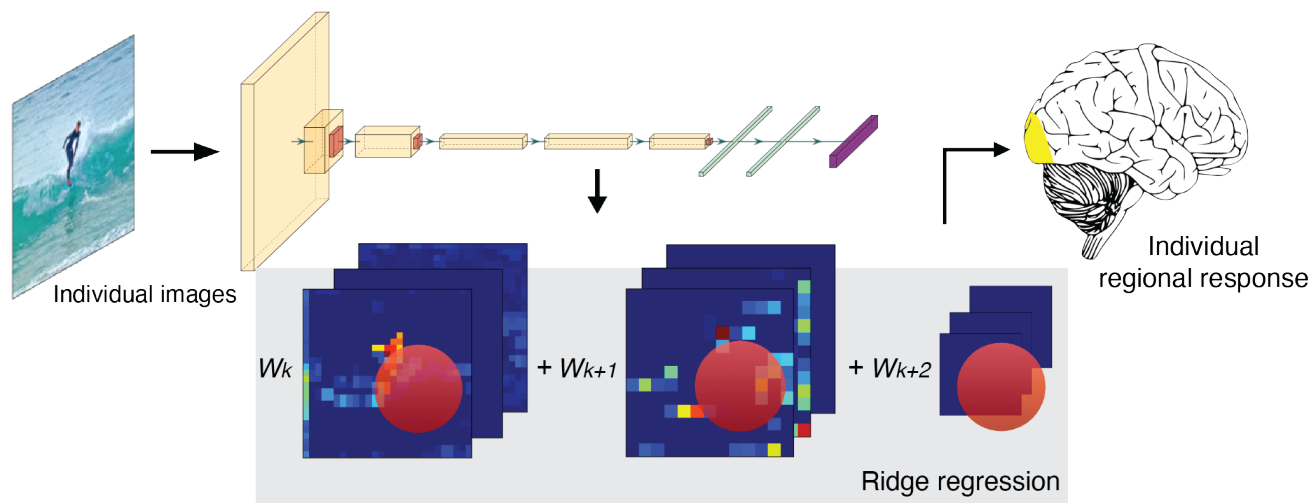


**Figure 1.** Framework of the Deepnet-fwRF encoding model. Image feature maps are extracted via convolutional and dense layers, followed by application of a Gaussian pooling field to reduce the feature maps to only those areas relevant to a specific region's responses. Finally, ridge regression is used to map the pooled features to the visual regions' responses.

Deepnet-fwRF encoding models were created for each of the 8 NSD individuals for 5 early to late visual regions - fusiform face area 1 (FFA1), early body area (EBA), parahippocampal place area (PPA), visual word form area 1 (VWFA1) and ventral V1 (V1v). Two types of individual-level encoding models were created: 1) individual-large models that were trained using all available data unique to an individual, which was on average 24,000 image-response pairs (and did not include the set of 1000 shared images) and 2) individual-small models that were trained on randomly selected subsets of image-response pairs, ranging in size from 10 to 800, drawn from the individual's unique set of 24,000 image-response pairs (not including the set of 1000 shared images). To obtain robust estimates of model performance, the individual-large and individual-small models were

tested on 100 randomly selected test sets of size 100 from the shared 1000 image-response pairs, see Table 1. These 100 sets of 100 test images varied across the model types (individual-large vs individual-small) but not across individuals' models within the same model type. Model performance metrics are reported as the mean value across the 100 test sets. To save compute time, the hyperparameters for the individual-small models (the Gaussian pooling center and radius) were fixed to the values obtained from individual-large model. If anything, this choice has the effect of inflating the accuracy of the individual-small models, as the Gaussian pooling parameters are fixed to their "optimal" value identified by the individual-large model.

### 2.2.2 Ensemble encoding models

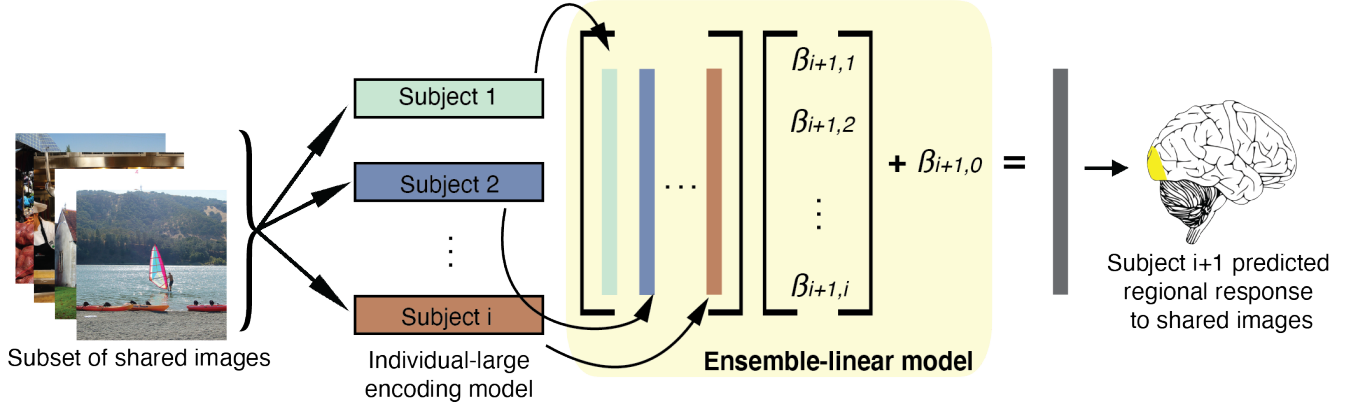


**Figure 2.** Ensemble-linear encoding models. The proposed ensemble-linear encoding models use the predicted responses from the individual-large encoding models of 7 subjects to predict the observed responses from the remaining 8th subject.

We created two ensemble encoding models that linearly combine the predictions from the 7 other subjects' individual-large encoding models to predict the 8th subject's regional response patterns, see 2. The first, called ensemble-average, uses the average predicted response of the other 7 individual-large models as the predicted response for the 8th individual. The second, called the ensemble-linear, predicts the 8th individual's response to image  $S$  using a linear model applied to the predictions from the other 7 NSD subjects' individual-large encoding models:

$$EL_i(S) = \beta_{i,0} + \sum_{j \in N_i} \beta_{i,j} \hat{r}_j(S) \quad (1)$$

where  $\beta_{i,0}$  is the intercept for individual  $i$ 's model,  $N_i$  indicates the set of indices not including individual  $i$ ,  $\beta_{i,j}$  is the coefficient for the  $j^{th}$  individual-large encoding model in predicting individual  $i$ 's responses and  $\hat{r}_j(S)$  is the predicted activation in response to image  $S$  for subject  $j$ 's individual-large encoding model. The ensemble-linear model was fitted and evaluated by splitting the shared set of 1000 image-response pairs into train and test sets 100 times. The training set size ranged from 10-800 while the test set was fixed at size 100 for consistency with the other model performance metrics, see Table 1. Model performance metrics are reported as the mean across these 100 random splits.

Model name	Train data			Test data		
	Source	Size	Repeats	Source	Size	Repeats
Individual-large	Unique 20K-27K	20,312 ~ 27,000	1	Shared 1000	100	100
Individual-small	Unique 20K-27K	10 – 800	100	Shared 1000	100	100
Ensemble-linear	Shared 1000, excluding test data	10 – 800	100	Shared 1000, excluding train data	100	100
Ensemble-average	N/A	N/A	N/A	Shared 1000	100	100

**Table 1.** List of encoding models and the source and size of their train and test data. "Unique 20K-27K" refers to the set of image-response pairs that were unique to each individual, while the "Shared 1000" refers to the set of 907 image-response pairs that were shown to all individuals. "Repeats" indicates the number of times the indicated set was randomly drawn. The 100 test sets of 100 image-response pairs was consistent across individuals within a model type.

### 2.3 Encoding model assessments

The individual-large models are considered here to be the gold standard reference model. Models were assessed in two ways - prediction accuracy and preservation of inter-individual variability. A model's prediction accuracy was calculated as the Pearson's correlation between the predicted and the measured responses across the 100 images in the test set; the average of this value across the 100 test sets is reported. The 100 test sets were consistent across individuals for a particular model type. Friedman tests with Dunn's corrections<sup>34</sup> for multiple comparisons were used to assess significant differences in prediction accuracy between the individual-small and ensemble-linear with the individual-large. A model's ability to preserve individual variability in image response patterns was assessed via inter-subject correlation (ISC) of the predicted responses across the 100 images in the test set; again, the average value across the 100 test sets is reported.

Importantly, we also measured the accuracy of the proposed ensemble encoding models, trained on the NSD dataset, on our prospectively collected NeuroGen dataset to assess robustness of the models to domain shift. The 480 image-response pairs for each individual were split into 80% training and 20% testing, making sure to select identical ratios of natural and synthetic image-response pairs. An ensemble-linear model was fit for each of the 6 NeuroGen's participants using their training data and the accuracy of the resulting model assessed using their test data. This process was repeated 100 times to obtain a robust estimate of model performance, i.e. average Pearson's correlation of observed versus predicted activity for the 100 test images, over the 100 repeated train/test splits.

#### 2.3.1 NeuroGen: activation optimized image synthesis

### NeuroGen

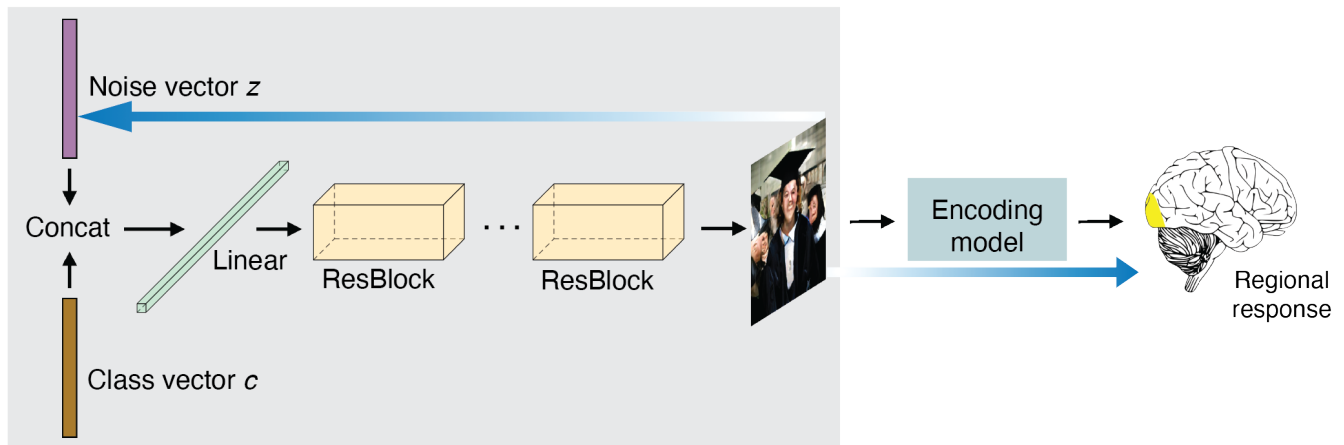


**Figure 3.** The NeuroGen framework concatenates an image generator with an encoding model to enable synthesis of images designed to achieve a desired activation pattern for a specific region(s).

We adopted the recently published NeuroGen framework, illustrated in Figure 3, which concatenates an image generator (BigGAN-deep<sup>35</sup>) with an encoding model to generate synthetic images predicted to optimally achieve a specific regional response pattern (i.e. maximize the response in a single region)<sup>18</sup>. In the previous version of NeuroGen, the individual-large encoding models were used to generate optimized images; here, we also test using the individual-small, ensemble-linear and ensemble-average encoding models. During optimal image generation, the one-hot encoded class vector is fixed and the gradient flows from the region's response back to the synthetic image's noise vector. The noise vector was sampled from a truncated normal distribution, with a truncation parameter of 0.4. The class vectors were identified as the 10 classes (out of the 1000 ImageNet classes) that produced an image - based on a random (unoptimized) noise vector - whose predicted regional activation was as close to the target activation as possible. We compared the synthetic images created from NeuroGen when using the various encoding models within the framework. Specifically, we tested if the individual variability in FFA1 responses to images containing dog and human faces that was previously identified via the NSD individual-large models<sup>18</sup> was preserved using the different encoding models. We also explored if this inter-individual variability in FFA1 responses could be identified and replicated using the NeuroGen framework applied to the prospective, novel individuals' personalized encoding models.

## 3 Results

### 3.1 Assessment of encoding models with NSD data

We constructed the above encoding models for five early and late visual regions: FFA1, EBA, PPA, VWFA1 and V1v. The individual-small and ensemble-linear encoding model accuracies when varying the size of the training data are provided in

Figure 4. For comparison, the individual-large accuracy is provided in green, after the break in the x-axis to indicate the size of the individuals' full sets of image-response pairs. Each boxplot illustrates the distribution of accuracy values over the 8 individuals in the NSD dataset. Test-retest reliability was calculated as the Pearson correlation between measured responses to two different viewings of the 1000 shared images; the mean and range across the 8 individuals is indicated by a dashed grey line and envelope, respectively.

### 3.2 Ensemble-linear performs better than individual-small and not different from individual-large

Unsurprisingly, the accuracies for both ensemble-linear and individual-small increase with training data size and both models only need 50 image-response pairs to surpass average test-retest reliability of measured responses. There is an obvious accuracy gap between ensemble-linear and individual-small when the number of training data is less than 400 and no significant differences in ensemble-linear and individual-large for any region when the training size exceeds 200 (Friedman tests with Dunn's corrected  $p > 0.05$ <sup>34</sup>).

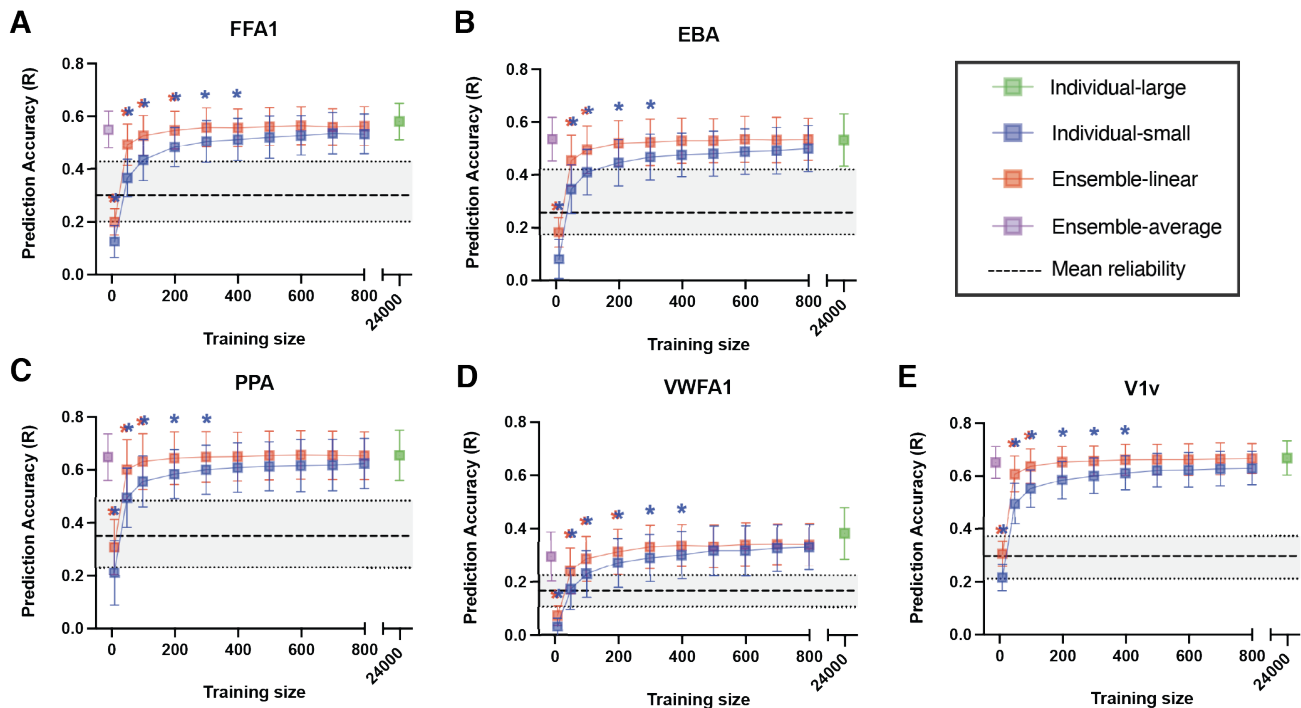


**Figure 4.** Boxplots indicate test accuracy across 8 individuals for the individual-small (blue) and ensemble-linear (red) models as training size increases from 10 to 800 image-response pairs. Each individual's accuracy is the mean across the 100 random draws of train/test image-response pairs for models with training size indicated on the x-axis. Individual-large accuracy across the 8 subjects is provided in green at a training size of 24K and the ensemble-average accuracy in purple at a training size of 0. Colored stars indicate a significant difference in that model from the gold-standard individual-large models. "Mean reliability" is calculated as the across-subject average of the Pearson correlation of two different measured responses to repeated viewings of the same set of 1000 shared images, with the gray envelope indicating the range of this value across the 8 individuals.

We perform a detailed comparison of the encoding model performances with a fixed training size of 400. A training size 400 was chosen because 1) it is reasonable amount of images that one participant can view during an hour-long MRI scan; 2) the ensemble-linear and individual-small model accuracies largely plateau at 400 for all regions. There was no statistical difference in accuracy between individual-large and ensemble-linear or ensemble-average models, except for the ensemble-average model having lower accuracy for VWFA1 (Friedmann's test, Dunnett correction for multiple comparisons). Individual-small had significantly lower accuracy for all regions compared to all other models except for VWFA1 where it was not significantly different from the ensemble-average model. This indicates the ensemble-linear model's ability to well approximate models trained on very large data (24K) with only a small amount of data (few hundred images) from a novel individual.

### 3.3 Ensemble-linear preserves inter-individual variability in predicted responses

An encoding model framework should not only be accurate, but it should also preserve inter-individual differences in response patterns as much as possible. Figure 5B illustrates our models' abilities to preserve inter-individual variability via ISC matrices

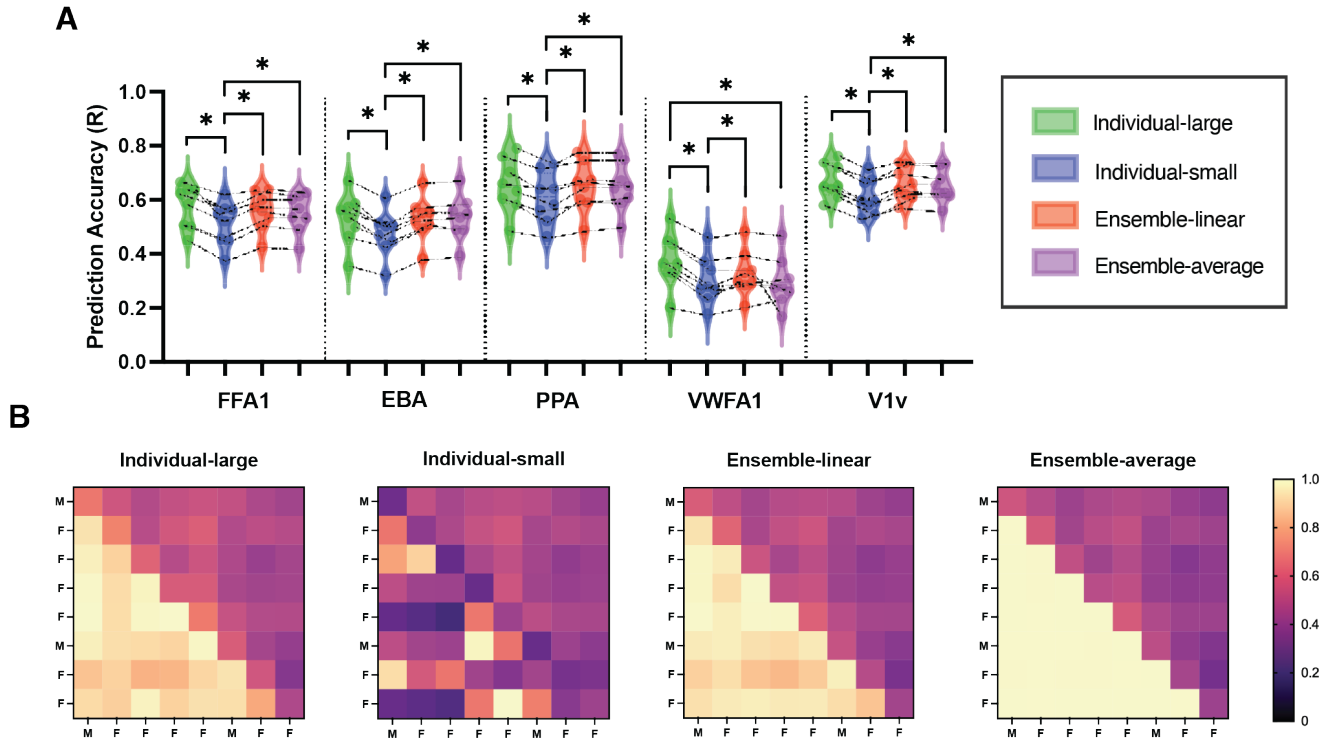


**Figure 5. A** Distribution of average model accuracies, calculated over 100 sets of 100 test images, for individual-large, individual-small, ensemble-linear and ensemble-average for eight NSD subjects when the image-response training size is 400. The same subject is connected via a grey dashed line. **B** Average inter-subject correlation (ISC) matrices of the predicted activation (lower triangular) and measured activation (upper triangular) for different encoding models across the 100 sets of 100 test images, averaged over the 5 regions of interest. Diagonals represent the average Pearson correlation between the predicted and measured activations over the 100 sets of 100 images for a given subject. Individuals' sexes are indicated for each row/column.

$C \in \mathbb{R}_{8 \times 8}$  where  $-1 \leq C_{i,j} \leq 1$  is the average Pearson correlation of the measured activations (upper triangular) and predicted activations (lower triangular) from subject  $i$  and subject  $j$  across the 100 sets of 100 test images; the diagonal is the average Pearson correlation of the predicted activations and measured activations for a given individual. Using the ISC of the measured activations as a gold standard, we observed that the individual-large model best preserves the pattern of inter-individual variability - its ISC matrix of predicted activations had the highest correlation with the measured activation ISC (Pearson's  $r = 0.62$ ,  $p = 4.18e - 4$ ). The ensemble-linear model also preserves the inter-individual variability at a level similar to that of the individual-large models (Pearson's  $r = 0.57$ ,  $p = 1.68e - 3$ ). Although the ensemble-average has relatively high prediction accuracy, it unsurprisingly has the lowest individual specificity and was not correlated with the measured activation ISC (Pearson's  $r = 0.10$ ,  $p = 0.62$ ). The individual-small model shows high individual specificity but its patterns did not match the measured activations' ISC (Pearson's  $r = -0.11$ ,  $p = 0.56$ ), likely due to the high level of noise in the predictions which also results in its poor accuracy. Out of the three models using small data, the ensemble-linear has the best balance of model accuracy and preservation of inter-individual differences, and, importantly, uses much less data than the individual-large model.

### 3.4 Synthetic images from the ensemble-linear models reflect inter-individual differences identified with the individual-large models

To demonstrate an application of the proposed ensemble approach, we use various encoding models to create optimized synthetic images within the NeuroGen framework. Specifically, we generated the 10 synthetic images predicted by different encoding models to maximize activation in the FFA1<sup>18</sup>. Figure 6 shows the 10 maximal FFA1 images for all 8 subjects (each subject in one row) for individual-large (panel A), ensemble-linear (panel B) and ensemble-average (panel C). The individual-small encoding model was not considered due to the low accuracy observed across all regions. We largely observe semantic content in the synthetic images that are expected from previous knowledge of the region in question, i.e. FFA1 maximal images all have faces (human and animal/dog). This validated the robustness of the NeuroGen approach to different

**A** Individual-large



**B** Ensemble-linear



**C** Ensemble-average

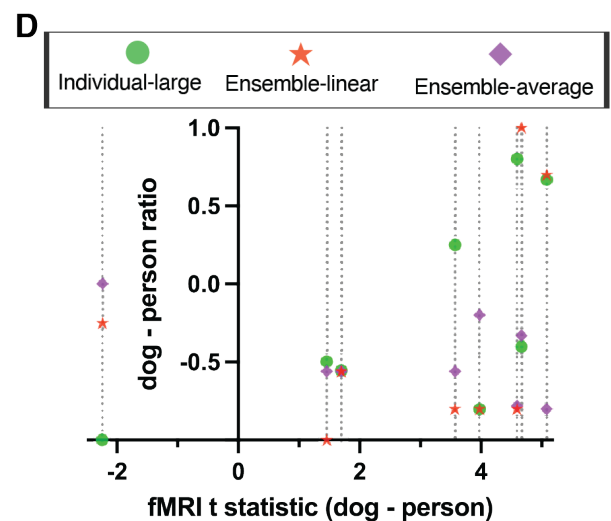


**Figure 6.** The 10 synthetic images predicted to achieve maximal activation for specific NSD individuals' FFA1, produced from the NeuroGen framework using **A** individual-large, **B** ensemble-linear and **C** ensemble-average encoding models. Subject-wise rows are arranged by the t-statistic of activation contrast in measured responses to dog faces versus human faces. **D** Scatter plot of the t-statistic for activation contrast to dog versus human faces for FFA1 (x-axis) and the number of dog faces minus the number of human faces divided by the total number of dog and human faces (y-axis) produced by NeuroGen using three different encoding models.



encoding models with varied levels of accuracy. Furthermore, our previous work validating NeuroGen used it to identify individually-varying levels of preference for dog faces versus human faces in the top 10 synthetic images that was significantly correlated with the t-statistic of the group difference in observed activation in response to dog vs human images<sup>18</sup>. This result was shown over all 8 individuals over 5 face areas; here we see that only looking at the 8 data points for FFA1's individual-large model results in a correlation that is almost significant ( $r = 0.69$ ,  $p = 0.06$ ). The dog-human ratio for FFA1's synthetic images generated using the ensemble-linear encoding model have a correlation that is also positive although not significant ( $r = 0.44$ ,  $p = 0.28$ ) but the correlation for the ensemble-average encoding model's synthetic images is actually negative ( $r = -0.51$ ,  $p = 0.21$ ), see Figure 6D. The correlations remain similar when using the top 100 synthetic images to calculate the ratio, again strengthening the point that individual differences can be reflected even in the top 10 synthetic images. We can see that subjects that do not have responses (and thus synthetic images) as close to the average of the 8 individuals will not have their individual variability as well preserved by the ensemble-average model.

### 3.5 External validation of the ensemble-linear encoding model

Finally, we assessed the effect of domain shift on the accuracy of the proposed ensemble-linear encoding model using our recently collected NeuroGen dataset. There are a few domain shifts between the NSD and NeuroGen datasets, including 1) different individuals, 2) different MRI scanner/strength (NSD having 7T vs NeuroGen having 3T) and fMRI parameters (TR, voxel size etc), 3) types of images used (NeuroGen used natural and synthetic images while NSD used only natural images) and 4) different images included in the test set used to calculate model accuracy. Retinotopic mapping was not performed in the NeuroGen experiment, so only the accuracy of the models in late visual areas FFA1, EBA, PPA and VWFA1 were tested. There was no significant drop in the ensemble-linear model's test accuracy from the NSD to the NeuroGen data for EBA and VWFA1, but there was a significant drop for FFA1 and PPA (corrected  $p < 0.05$  via a Mann-Whitney test), see Figure 7A. There was also no difference in the ensemble-linear model's performance on the natural and synthetic images within the NeuroGen data. Inter-subject correlation of the predicted responses are shown in Figure 7B and confirm that the ensemble-linear model still maintains a level of individual variability within the NeuroGen data similar to that observed in the NSD data. Importantly, the pattern of ISC for the ensemble-linear model's predicted activations has a level of correspondence with the measured activations' ISC (Pearson's  $r = 0.59$ ,  $p = 0.02$ ) similar to that observed in the NSD data. One interesting observation is that the only male participant in the prospective NeuroGen experiments had very different encoding model predictions compared to the other 5 female participants, which is also reflected in the ISC of the measured activations.

When applying the NeuroGen framework using the novel individual's ensemble-linear encoding models, we observe a qualitative relationship between the FFA1's level of measured preference for animal versus human faces and the ratio of animal versus human faces in the top 10 synthetic images, see Figure 3C. We extended the category from only dogs (as in the NSD analysis) to include dogs plus other animal faces due to the small number of observed brain responses to images used to calculate a t-statistic. Figure 3D shows a positive linear trend between the animal versus human face preference ratio in the synthetic images and the t-statistic of the observed activation in response to dog versus human faces for the six NeuroGen individuals. Most individuals are in the upper right or lower left quadrants indicating general agreement of the dog vs human preference in the synthetic images and observed responses. The individuals' FFA1 encoding model accuracies are illustrated by the color of the point; we see that the individual with the worst agreement in the t-statistic and synthetic image ratios (lower right quadrant) also has the lowest accuracy in the encoding model. Using accuracy-weighted correlation, a positive trend between the t-statistic and the ratios was identified ( $r = 0.62$ ,  $p = 0.15$ ). These results demonstrate the relatively robust nature of the NeuroGen framework for discovering inter-individual differences in neural representations of visual stimuli in novel individuals.

## 4 Discussion

Here we propose a visual encoding model framework that linearly combines outputs from several individuals' existing encoding models (trained on densely-sampled NSD data) to predict a novel individual's brain responses to a given image. We show that the proposed ensemble-linear model, trained using a relatively small number of image-response pairs for a novel individual (400, roughly equivalent to 40 minutes of fMRI), achieves accuracy similar to encoding models trained on a very large number of image-response pairs from that individual (24K, roughly 35-40 hours of fMRI). Importantly, the ensemble-linear models preserved a pattern of inter-individual variability in responses that was similar to the pattern observed from the encoding models trained on the large data. In the context of NeuroGen, a synthetic image generator previously proposed as a tool for discovery neuroscience, the ensemble-linear model reproduced the individual variability in the content of synthetic images designed to maximize activation in FFA1. Finally, we validated the accuracy of the ensemble-linear model on prospectively collected data; despite several domain shifts we only saw a significant drop in accuracy for two regions and synthetic images did not have significantly different accuracy compared to natural ones. We also provide preliminary evidence suggesting that the inter-individual variability in FFA1 responses to dogs and humans was replicated in the synthetic images generated via

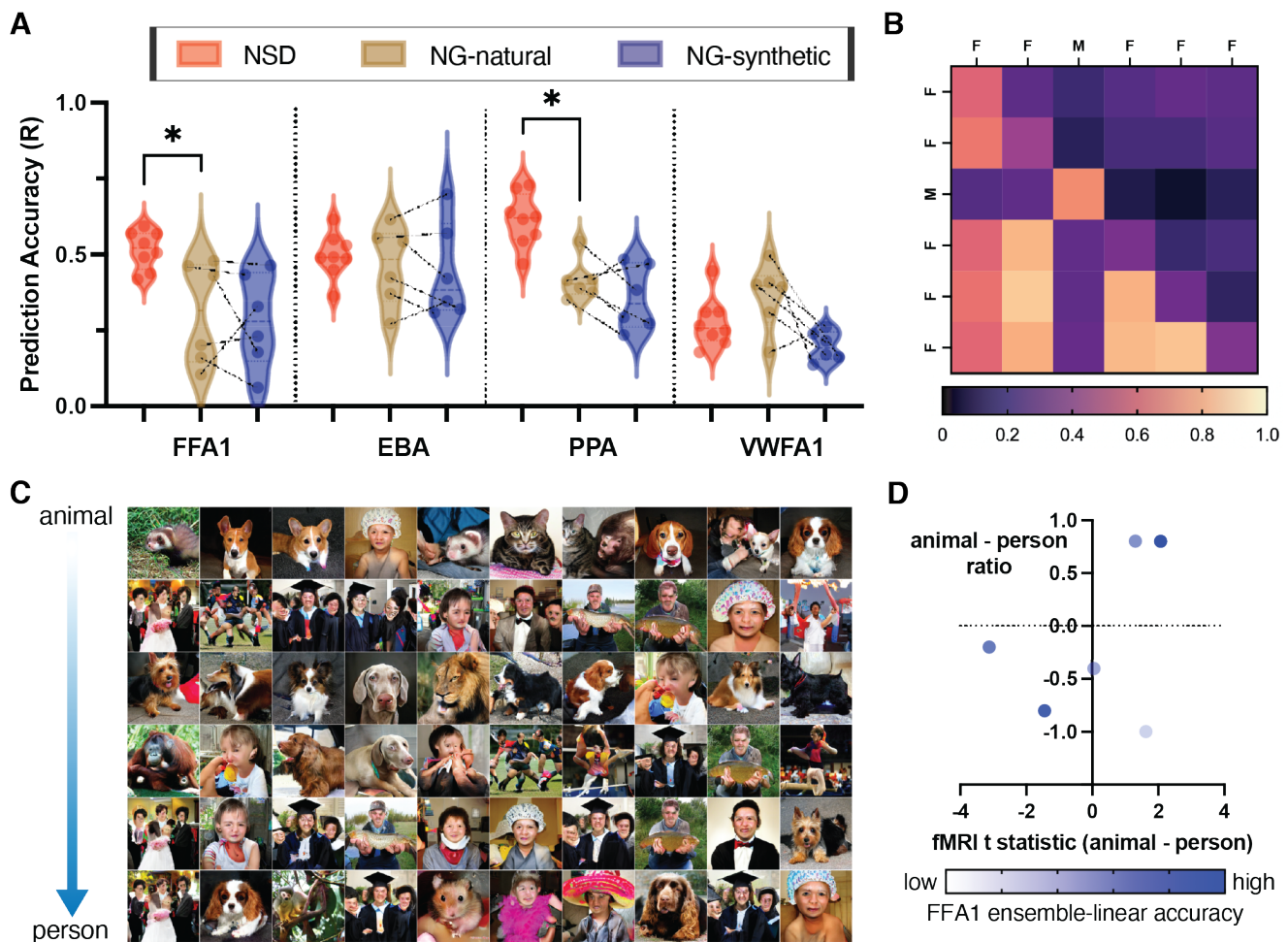


**Figure 7.** Ensemble-linear model performance on prospective NeuroGen data. **A** Prediction accuracy for the ensemble-linear encoding model trained on NSD individuals' data and tested on i) NSD individuals' responses to natural images (NSD), ii) NeuroGen individuals' responses to natural images (NG-natural) and iii) NeuroGen individuals' responses to synthetic images (NG-synthetic) for regions FFA1, EBA, PPA and VWFA1. **B** The lower triangular portion shows the inter-subject correlation of the ensemble-linear model's predicted activations, the upper triangular portion shows the inter-subject correlation of the measured activations and the diagonal is the correlation between predicted activations and measured activations for the six NeuroGen individuals, averaged over the 4 regions of interest. **C** The top 10 synthetic images designed to maximize activation in FFA1 for each of the NeuroGen individuals (one individual per row), arranged by the t-statistic indicating the contrast of measured activity in response to animal faces compared to human faces (animal preference at top, human preference at bottom). **D** A scatter plot indicating for each of the NeuroGen individuals, i) the observed t-statistic of FFA1's responses to animal versus human face images and ii) the ratio of the number of animal images minus the number of human images, divided by the sum of these two numbers, in their top 10 synthetic images. The points are colored by the accuracy of the FFA1 ensemble-linear encoding model for that individual, where white is lower and dark blue is higher.

NeuroGen using the ensemble-linear encoding model for the prospectively scanned individuals. These results suggest that the ensemble-linear framework can be used to efficiently create accurate, individually personalized encoding models and optimized synthetic images for prospective vision experiments.

Neural encoding and decoding models have long been used to characterize and predict how sensory, cognitive or motor information is spatially represented in the brain<sup>1,36,37</sup>. Recent work has revealed that understanding the inter-individual differences in responses to naturalistic stimuli may shed light on behavioral or pathological variability in humans<sup>19,20,38</sup> and monkeys<sup>39</sup>. Having high-quality and large-scale stimuli-response data is critical to building accurate and useful encoding or decoding models, but due to the massive cost in time and resources there are only a few such datasets available<sup>2,22</sup>. Retrospective analyses of these datasets are constrained by the original parameters of the experiment and the characteristics of the stimuli presented within them. If it is not possible to test a specific hypothesis with the existing data, scientists will need to collect new data on novel individuals. Our proposed approach aims to bootstrap existing large-scale datasets to improve the starting point of these prospective experiments by providing a more accurate baseline visual encoding model that also preserves inter-individual variability response patterns. Furthermore, we provide quantitatively derived guidelines for how many images are needed to achieve accuracy similar to encoding models trained on very large-scale data.

Linear models, with their simplicity and desirable statistical properties, have been a fundamental statistical/machine learning approach<sup>40</sup> with many applications in network, cognitive, visual neuroscience<sup>23,41,42</sup>. The gold-standard validation of statistical or machine learning models is demonstrating its accuracy is robust to domain or distribution shift of the underlying data<sup>43</sup>, which we set out to do for our ensemble-linear approach. Here, the shift happens in three major ways - first is the data acquisition (scanner, scanner strength, repetition time, voxel size, etc.), second is the individuals undergoing the experiments were not identical and the third was the type of images shown to the individuals during the scan (natural versus natural and synthetic). Despite these several major shifts in data characteristics, there was not a significant drop in accuracy for the EBA and VWFA1 models, while for FFA1 and PPA the gap was significant. Considering the number and nature of the domain shifts, we considered the fact that not all regions lost accuracy to be somewhat of a validation - it should be considered, however, that some regions may be more robust to domain shift than others. Future work could explore using non-linear ensemble modeling that may allow better preservation of accuracy across varied experimental conditions.

Our previously developed NeuroGen framework<sup>18</sup> was used to generate synthetic images that were predicted by a given encoding model to achieve a targeted pattern of activity in a specific brain region. Unlike similar frameworks developed for monkey or mouse models<sup>44-46</sup>, it is difficult to directly optimize stimuli for humans in real time while they are undergoing fMRI. An achievable alternative may be to fine-tune our ensemble-linear model for a prospective individual using image-response data collected at the first scan, which could then be plugged into the NeuroGen framework to create personalized, optimal synthetic images that could be shown to that same individual during a second scan. In this setup, if the ensemble-linear encoding model does not accurately predict responses to synthetic images then the NeuroGen framework will fail. Our current results demonstrating that the ensemble-linear model does just as well on predicting responses to natural and synthetic images is thus an essential part of prospective experiments utilizing NeuroGen.

Interestingly, we demonstrated that the ensemble-linear encoding models applied to the NSD individuals preserved somewhat the previous finding of inter-individual variability in FFA1 responses to images of dog faces compared to human faces<sup>18</sup>. While the correlation was not significant, we did see a trend suggesting that the inter-individual preference in FFA1 for dog versus human faces was replicated with the NeuroGen framework utilizing the personalised ensemble-linear models for the prospective NeuroGen individuals, despite the fact that the FFA1 model had a significant drop in accuracy. This demonstrates the robustness of the NeuroGen framework to drops in accuracy of the encoding model used within, and suggests that our previously identified inter-individual variability in face area responses to images containing dog versus human faces can be replicated in novel individuals.

## 5 Conclusion

This work proposes and validates an ensemble framework that uses previously collected, deeply sampled data to efficiently create accurate, personalized encoding models and, subsequently, optimized synthetic images for novel individuals. Importantly, we validate that the encoding models can be applied to a certain extent in novel experimental conditions and that they did not have different accuracy for predicting responses to natural versus synthetic images. Future work will use this framework to investigate inter-individual differences in visual encoding and create personalized synthetic images designed to achieve a targeted pattern of brain activity within a specific individual.

## Data availability

The Natural Scene Dataset (NSD) is publicly available at <http://naturalscenesdataset.org>.

## Code availability

Code is available at <https://github.com/zijin-gu/NeuroGen>.

## Ethics statement

All studies were approved by an ethical standards committee on human experimentation, and written informed consent was obtained from all participants.

## References

1. Naselaris, T., Kay, K. N., Nishimoto, S. & Gallant, J. L. Encoding and decoding in fmri. *Neuroimage* **56**, 400–410 (2011).
2. Allen, E. J. *et al.* A massive 7t fmri dataset to bridge cognitive neuroscience and artificial intelligence. *Nat. neuroscience* 1–11 (2021).
3. Krizhevsky, A., Sutskever, I. & Hinton, G. E. Imagenet classification with deep convolutional neural networks. *Adv. neural information processing systems* **25**, 1097–1105 (2012).
4. Girshick, R., Donahue, J., Darrell, T. & Malik, J. Rich feature hierarchies for accurate object detection and semantic segmentation. In *Proceedings of the IEEE conference on computer vision and pattern recognition*, 580–587 (2014).
5. Simonyan, K. & Zisserman, A. Very deep convolutional networks for large-scale image recognition. *arXiv preprint arXiv:1409.1556* (2014).
6. Sermanet, P. *et al.* Overfeat: Integrated recognition, localization and detection using convolutional networks. *arXiv preprint arXiv:1312.6229* (2013).
7. LeCun, Y., Bengio, Y. & Hinton, G. Deep learning. *nature* **521**, 436–444 (2015).
8. Wen, H. *et al.* Neural encoding and decoding with deep learning for dynamic natural vision. *Cereb. cortex* **28**, 4136–4160 (2018).
9. Schrimpf, M. *et al.* Brain-score: Which artificial neural network for object recognition is most brain-like? *BioRxiv* 407007 (2020).
10. Rosenblatt, F. The perceptron: a probabilistic model for information storage and organization in the brain. *Psychol. review* **65**, 386 (1958).
11. DiCarlo, J. J., Zoccolan, D. & Rust, N. C. How does the brain solve visual object recognition? *Neuron* **73**, 415–434 (2012).
12. DeAngelis, G. C., Ohzawa, I. & Freeman, R. D. Receptive-field dynamics in the central visual pathways. *Trends neurosciences* **18**, 451–458 (1995).
13. De Valois, R. L. & De Valois, K. K. Spatial vision. *Annu. review psychology* **31**, 309–341 (1980).
14. Kanwisher, N., McDermott, J. & Chun, M. M. The fusiform face area: a module in human extrastriate cortex specialized for face perception. *J. neuroscience* **17**, 4302–4311 (1997).
15. Downing, P. E., Jiang, Y., Shuman, M. & Kanwisher, N. A cortical area selective for visual processing of the human body. *Science* **293**, 2470–2473 (2001).
16. Epstein, R. & Kanwisher, N. A cortical representation of the local visual environment. *Nature* **392**, 598–601 (1998).
17. Kim, J. S., Kanjlia, S., Merabet, L. B. & Bedny, M. Development of the visual word form area requires visual experience: Evidence from blind braille readers. *J. Neurosci.* **37**, 11495–11504 (2017).
18. Gu, Z. *et al.* Neurogen: activation optimized image synthesis for discovery neuroscience. *NeuroImage* **247**, 118812 (2022).
19. Finn, E. S., Corlett, P. R., Chen, G., Bandettini, P. A. & Constable, R. T. Trait paranoia shapes inter-subject synchrony in brain activity during an ambiguous social narrative. *Nat. Commun.* **9**, 2043, DOI: [10.1038/s41467-018-04387-2](https://doi.org/10.1038/s41467-018-04387-2) (2018).
20. Finn, E. S. & Bandettini, P. A. Movie-watching outperforms rest for functional connectivity-based prediction of behavior. *NeuroImage* **235**, 117963 (2021).
21. Kay, K. N., Naselaris, T., Prenger, R. J. & Gallant, J. L. Identifying natural images from human brain activity. *Nature* **452**, 352–355 (2008).
22. Van Essen, D. C. *et al.* The wu-minn human connectome project: an overview. *Neuroimage* **80**, 62–79 (2013).
23. Yamins, D. L. & DiCarlo, J. J. Using goal-driven deep learning models to understand sensory cortex. *Nat. neuroscience* **19**, 356–365 (2016).

24. Güçlü, U. & van Gerven, M. A. Deep neural networks reveal a gradient in the complexity of neural representations across the ventral stream. *J. Neurosci.* **35**, 10005–10014 (2015).
25. Cichy, R. M., Khosla, A., Pantazis, D., Torralba, A. & Oliva, A. Comparison of deep neural networks to spatio-temporal cortical dynamics of human visual object recognition reveals hierarchical correspondence. *Sci. reports* **6**, 1–13 (2016).
26. Khosla, M., Ngo, G. H., Jamison, K., Kuceyeski, A. & Sabuncu, M. R. Cortical response to naturalistic stimuli is largely predictable with deep neural networks. *bioRxiv* (2020).
27. St-Yves, G. & Naselaris, T. The feature-weighted receptive field: an interpretable encoding model for complex feature spaces. *NeuroImage* **180**, 188–202 (2018).
28. Lin, T.-Y. *et al.* Microsoft coco: Common objects in context. In *European conference on computer vision*, 740–755 (Springer, 2014).
29. Charest, I., Kriegeskorte, N. & Kay, K. N. Glmdenoise improves multivariate pattern analysis of fmri data. *NeuroImage* **183**, 606–616 (2018).
30. Kay, K., Rokem, A., Winawer, J., Dougherty, R. & Wandell, B. Glmdenoise: a fast, automated technique for denoising task-based fmri data. *Front. neuroscience* **7**, 247 (2013).
31. Rokem, A. & Kay, K. Fractional ridge regression: a fast, interpretable reparameterization of ridge regression. *GigaScience* **9**, giaa133 (2020).
32. Andersson, J. L., Skare, S. & Ashburner, J. How to correct susceptibility distortions in spin-echo echo-planar images: application to diffusion tensor imaging. *Neuroimage* **20**, 870–888 (2003).
33. Russakovsky, O. *et al.* Imagenet large scale visual recognition challenge. *Int. journal computer vision* **115**, 211–252 (2015).
34. Upton, G. & Cook, I. *A dictionary of statistics 3e* (Oxford university press, 2014).
35. Brock, A., Donahue, J. & Simonyan, K. Large scale gan training for high fidelity natural image synthesis. *arXiv preprint arXiv:1809.11096* (2018).
36. VanRullen, R. & Reddy, L. Reconstructing faces from fMRI patterns using deep generative neural networks. *Commun. Biol.* **2**, 193, DOI: [10.1038/s42003-019-0438-y](https://doi.org/10.1038/s42003-019-0438-y) (2019).
37. Ratan Murty, N. A., Bashivan, P., Abate, A., DiCarlo, J. J. & Kanwisher, N. Computational models of category-selective brain regions enable high-throughput tests of selectivity. *Nat. Commun.* **12**, 5540, DOI: [10.1038/s41467-021-25409-6](https://doi.org/10.1038/s41467-021-25409-6) (2021).
38. Petrican, R., Graham, K. S. & Lawrence, A. D. Brain-environment alignment during movie watching predicts fluid intelligence and affective function in adulthood. *NeuroImage* 118177 (2021).
39. Cowley, B. R. *et al.* Slow drift of neural activity as a signature of impulsivity in macaque visual and prefrontal cortex. *Neuron* **108**, 551–567.e8, DOI: <https://doi.org/10.1016/j.neuron.2020.07.021> (2020).
40. Matloff, N. *Statistical regression and classification: from linear models to machine learning* (CRC Press, 2017).
41. Gu, Z., Jamison, K. W., Sabuncu, M. R. & Kuceyeski, A. Heritability and interindividual variability of regional structure-function coupling. *Nat. Commun.* **12**, 1–12 (2021).
42. Piray, P. & Daw, N. D. Linear reinforcement learning in planning, grid fields, and cognitive control. *Nat. Commun.* **12**, 1–20 (2021).
43. Sun, B., Feng, J. & Saenko, K. Return of frustratingly easy domain adaptation. In *Proceedings of the AAAI Conference on Artificial Intelligence*, vol. 30 (2016).
44. Bashivan, P., Kar, K. & DiCarlo, J. J. Neural population control via deep image synthesis. *Science* **364** (2019).
45. Ponce, C. R. *et al.* Evolving images for visual neurons using a deep generative network reveals coding principles and neuronal preferences. *Cell* **177**, 999–1009 (2019).
46. Walker, E. Y. *et al.* Inception loops discover what excites neurons most using deep predictive models. *Nat. neuroscience* **22**, 2060–2065 (2019).
47. Dworkin, J. D. *et al.* The extent and drivers of gender imbalance in neuroscience reference lists. *Nat. Neurosci.* **23**, 918–926 (2020).

## **Acknowledgements**

This work was funded by the following grants: R01 NS102646 (AK), RF1 MH123232 (AK), R01 LM012719 (MS), R01 AG053949 (MS), NSF CAREER 1748377 (MS), NSF NeuroNex Grant 1707312 (MS), and Cornell/Weill Cornell Intercampus Pilot Grant (AK and MS). The NSD data were collected by Kendrick Kay and Thomas Naselaris under the NSF CRCNS grants IIS-1822683 and IIS-1822929.

## **Author contributions statement**

Zijin Gu: Methodology, Software, Validation, Formal analysis, Writing - Original Draft, Writing - Review & Editing. Keith Wakefield Jamison: Conceptualization, Methodology, Software, Formal Analysis, Writing - Review & Editing. Mert Sabuncu: Conceptualization, Methodology, Supervision, Writing - Review & Editing. Amy Kuceyeski: Conceptualization, Methodology, Supervision, Writing - Original Draft, Writing - Review & Editing.

## **Citation gender diversity statement**

Recent work in several fields of science has identified a bias in citation practices such that papers from women and other minorities are under-cited relative to the number of such papers in the field<sup>47</sup>. Here we sought to proactively consider choosing references that reflect the diversity of the field in thought, form of contribution, gender, and other factors. We obtained predicted gender of the first and last author of each reference by using databases that store the probability of a name being carried by a woman<sup>47</sup>. By this measure (and excluding self-citations to the first and last authors of our current paper), our references contain 5.12% woman(first)/woman(last), 26.37% man/woman, 15.48% woman/man, and 53.02% man/man. This method is limited in that a) names, pronouns, and social media profiles used to construct the databases may not, in every case, be indicative of gender identity and b) it cannot account for intersex, non-binary, or transgender people. We look forward to future work that could help us to better understand how to support equitable practices in science.